Phase Space Reframing for Directed Fusion Exhaust: A Concept Paper on Proton-Boron (p-^{11}B) Propulsion

for Near-Term Research Prioritization

Tyler Martin
Lobster Labs
Madrid, Spain
April 2026

Abstract

This concept paper identifies a performance regime for fusion propulsion that has not been systematically explored: direct magnetic collimation of non-thermal proton-boron (p-^{11}B) fusion products, exploiting the asymmetric entropy structure of the three-alpha final state. We argue that p-^{11}B products occupy a region of phase space where entropy is concentrated primarily in angular distribution, while momentum magnitude remains narrowly bounded at the MeV scale. Under Liouville's theorem, magnetic nozzle geometries can trade angular dispersion for spatial dispersion without reducing phase space volume. Because propulsion depends only on axial momentum and is indifferent to the spatial spread of the exhaust, this trade is favorable in principle. Adiabatic analysis indicates that collimation is physically effective at mirror ratios up to approximately 10, where particles undergo non-adiabatic detachment with most perpendicular energy already converted to parallel motion. The resulting directional efficiencies of 70–90% yield estimated propellant mass fractions of 28–31% for a 10-day Earth-Jupiter brachistochrone transfer. These estimates identify a target design space, not a demonstrated performance level. We specify the simulation and experimental work required to validate or bound the concept, catalog the engineering research directions suitable for autonomous research systems, and situate the work within the broader context of propulsion infrastructure for an era of accelerating research capability.

Keywords: *proton-boron fusion, aneutronic propulsion, phase space, Liouville's theorem, magnetic nozzle, adiabatic invariant, directed exhaust, interplanetary propulsion, autonomous research*

1. Introduction

1.1 The Propulsion Gap

The distances between the inner planets are not large by the standards of nuclear energy. Earth to Mars at opposition is roughly 0.5 AU; Earth to Jupiter is roughly 5 AU. Fusion reactions release approximately six orders of magnitude more energy per unit mass than chemical combustion. In principle, fusion-powered spacecraft could reduce interplanetary transit times from months to days, transforming space transport from expedition logistics to routine operations.

No fusion propulsion system has been built or tested at any scale. The reasons are partly engineering (plasma confinement, ignition thresholds, materials) and partly thermodynamic. This paper addresses the thermodynamic obstacle, which has received less systematic attention.

1.2 Why This Matters Now

The motivation for this work is grounded in a specific development: the rapid acceleration of autonomous research capability. The arrival of artificial general intelligence (AGI) and, in foreseeable succession, artificial superintelligence (ASI) will transform the pace of scientific and engineering research. Problems requiring decades of incremental human-led laboratory work may become tractable on timescales of years, once autonomous systems can design experiments, interpret results, and iterate without the bottleneck of human cognitive bandwidth.

Fusion ignition is one of the hardest remaining engineering problems. Proton-boron fusion, with its extreme ignition temperature (~300 keV), is harder still. But the difficulty is primarily a confinement and plasma control problem: exactly the kind of high-dimensional optimization where autonomous research systems are most likely to achieve rapid breakthroughs. Companies including TAE Technologies (field-reversed configurations), HB11 Energy (laser-driven approaches), and ENN (spherical torus) are already pursuing p-^{11}B fusion. The question this paper addresses is: assuming ignition is achieved, what performance regime does p-^{11}B open for propulsion, and is that regime worth targeting?

The answer matters for infrastructure planning. If p-^{11}B directed exhaust can deliver the performance estimated here, the downstream engineering (magnetic nozzle design, thermal management, fuel handling) should be studied in parallel with ignition research, not deferred until ignition is demonstrated. The propulsion architecture and the fusion core are separable problems. Solving them sequentially wastes the time advantage that accelerated research capability provides.

1.3 The Strategic Context

Multiple actors are building toward sustained human presence beyond Earth orbit. SpaceX’s Starship architecture targets launch costs enabling large-scale orbital and cislunar construction. Proposals for lunar and Martian industrial operations are advancing from concept to early engineering. The missing element is fast, efficient interplanetary transport. Chemical propulsion can reach Mars, but transit times (6–9 months) and mass ratios (>90% propellant) constrain mission architecture to the point where permanent industrial presence requires enormous logistical overhead.

A propulsion system delivering ~0.4g continuous acceleration with propellant fractions below 35% would change this calculus. Transit times to Mars drop to days. Jupiter becomes reachable in weeks. The asteroid belt, Jovian moons, and outer solar system become accessible for industrial operations.

The propellant fractions estimated in this paper (28–31%) are compatible with routine, reusable interplanetary transport in a way that conventional fusion concepts (60–97% propellant) are not. At these mass fractions, permanent bases, mining operations, and industrial facilities across the solar system become logistically supportable rather than requiring expedition-scale commitment for every resupply.

The convergence is specific: ASI-enabled research systems on Earth solve the ignition problem through hypercompressed engineering iteration; directed exhaust architecture converts that breakthrough into propulsion performance that existing concepts cannot match; and that performance enables the interplanetary industrial expansion that multiple actors are already building toward. Each link requires research now, because the timeline for AGI/ASI arrival is measured in years, not decades.

1.4 Scope and Limitations

This is a concept paper, not a design study. It identifies a performance regime, argues that the physics permits it, estimates its parametric sensitivity, and specifies what further work is needed. It does not present transport simulations, particle-tracing results, or engineering designs. Quantitative estimates should be understood as defining a target design space, not predicting system performance.

The central claim is narrow: p-^{11}B fusion products have an entropy structure qualitatively more favorable for direct magnetic collimation than thermal plasmas, and this has not been properly exploited or clearly articulated in the existing literature.

2. Theoretical Framework

2.1 Liouville's Theorem and Propulsion

A system of N particles in three dimensions occupies a volume in 6N-dimensional phase space. Liouville's theorem states that the phase space density is constant along Hamiltonian trajectories:

$$d\rho/dt = \partial\rho/\partial t + \{\rho, H\} = 0 \quad (1)$$

The volume occupied by a collection of particles in phase space is invariant under lossless dynamics. The standard conclusion is that fusion exhaust cannot be collimated without dissipating entropy or discarding particles.

This conclusion is correct about full phase space volume. But propulsion does not require compression of all phase space dimensions. It requires only that momentum vectors align along the thrust axis. The spatial distribution of the exhaust is irrelevant to thrust. This distinction is routine in accelerator physics (beam emittance trades) but has not been systematically applied to fusion propulsion.

2.2 Phase Space Structure of p-^{11}B Products

The proton-boron fusion reaction:

$$p + {}^{11}B \rightarrow 3\alpha + 8.7\ MeV \quad (2)$$

produces three alpha particles (rest mass 3727.4 MeV/c² each) sharing 8.7 MeV of kinetic energy. The reaction proceeds predominantly through an intermediate ^{8}Be* state: one alpha is emitted promptly with high energy (~4–5 MeV), and the remaining ^{8}Be* decays into two alphas at lower energy (~1.5 MeV each). The resulting energy distribution is not Gaussian but bimodal, with structure visible in the Dalitz plot [16, 17]. The mean kinetic energy per alpha is approximately 2.9 MeV, but individual alphas span a range from roughly 1.5 to 5 MeV.

This bimodal structure has a specific consequence for collimation: the high-energy prompt alpha (~5 MeV) has a larger Larmor radius than the ^{8}Be* decay alphas (~1.5 MeV) by a factor of roughly $\sqrt{(5/1.5)} \approx 1.8$. It will therefore reach the adiabatic breakdown threshold ($\varepsilon \approx 1$) earlier in the nozzle expansion, detaching at a lower effective mirror ratio with a wider pitch angle. The exhaust is not a single population with ±25% spread; it is two populations with different collimation characteristics. The directional efficiency estimates in Section 4 should be understood as averages over this bimodal distribution, and the actual performance will depend on the relative weighting of the prompt and sequential channels. Proper quantification requires particle tracing using the measured differential cross-sections [16, 17] as initial conditions.

The mean velocity for a 2.9 MeV alpha is:

$$v_a = c\sqrt{(1 - 1/(1 + T/m_a c^2)^2)} \approx 0.039c \approx 11{,}700\ km/s \quad (3)$$

Despite the bimodal energy structure, the velocity spread remains qualitatively different from a Maxwellian plasma: the alphas occupy a bounded energy range (1.5–5 MeV) rather than the factor-

of-several spread typical of thermal distributions. The angular distribution is approximately isotropic (4π steradians) in the lab frame.

The occupied phase space decomposes schematically as:

$$\Gamma \sim \Delta V \times \Delta p\_r \times \Delta\Omega \quad (4)$$

where Δp_r (momentum magnitude spread) is narrow relative to the mean, while ΔΩ (solid angle) approaches its maximum. The entropy is dominated by the angular term. This is the key observation: the phase space is concentrated in the angular subspace, which is exactly the subspace magnetic fields act on.

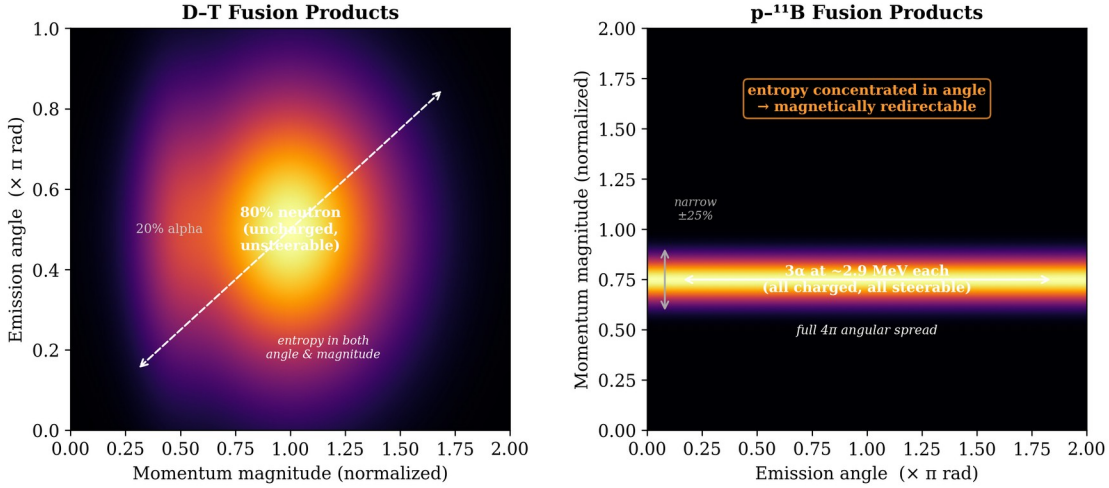

Figure 2. *Phase space distributions of D–T and p-¹¹B fusion products. Left: D–T products occupy a broad region in both momentum magnitude and emission angle, with 80% of the energy in uncharged neutrons. Right: p-¹¹B products form a narrow band in momentum magnitude (±25% spread from three-body kinematics) but span the full 4π solid angle. The entropy is concentrated entirely in the angular dimension, which is the dimension magnetic fields can act on.*

2.3 The Collimation-Position Trade

A diverging magnetic field redirects charged particle trajectories through conservation of the adiabatic invariant (magnetic moment μ = mv⊥²/2B). As particles enter weaker field regions, transverse velocity converts to parallel velocity while the spatial distribution broadens:

$$\Delta p\_\perp \times \Delta x\_\perp \geq constant \quad (5)$$

For propulsion this trade is favorable: thrust depends on total axial momentum flux integrated over the exhaust cross-section, and a spatially broad but well-collimated exhaust delivers the same thrust as a narrow one.

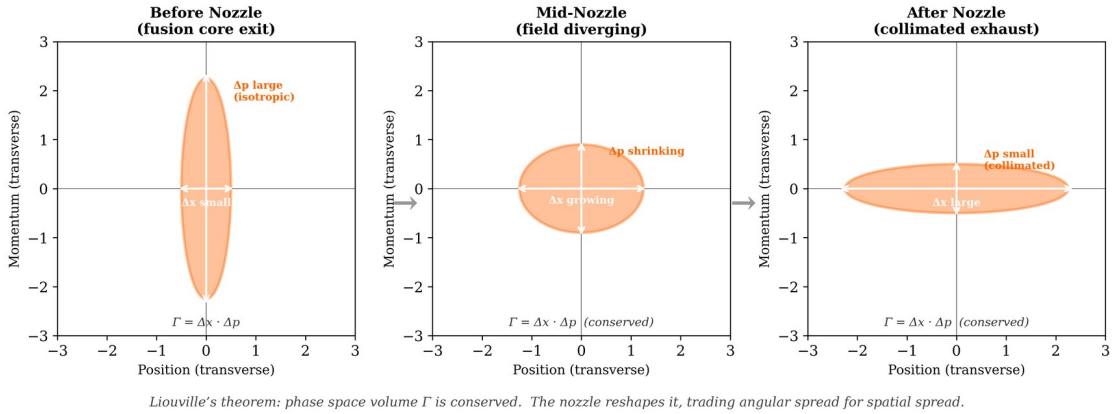

Figure 3. *The collimation-position trade under Liouville's theorem. The phase space volume Γ = Δx · Δp is conserved through the nozzle. At the fusion core exit (left), the distribution is narrow in position but broad in transverse momentum (isotropic emission). The diverging magnetic field reshapes the distribution (center) until, at the nozzle exit (right), the transverse momentum spread is small (collimated) and the position spread is large. The total phase space area is unchanged. Since propulsion depends only on momentum alignment, not spatial distribution, the constraint falls on an irrelevant degree of freedom.*

2.4 Adiabatic Limits and Detachment

The adiabatic invariant is conserved only when the field varies slowly over a single Larmor orbit. The adiabaticity parameter is:

$$\varepsilon = r_L / L_B \quad (6)$$

where r_L is the Larmor radius and L_B = |B/∇B| is the field gradient scale length. Adiabaticity requires $\varepsilon \ll 1$. For a 2.9 MeV alpha (He^{2+}), the magnetic rigidity gives:

$$r_L \approx 0.24/B \text{ meters} \quad (7)$$

where B is in Tesla. At a nozzle throat field of 10 T, r_L ≈ 2.4 cm and the particle is well-confined. As the field drops through the expansion, the Larmor radius grows. For a nozzle with gradient scale length L_B ≈ 2 m:

At 10 T: r_L ≈ 0.024 m, ε ≈ 0.012. Fully adiabatic.

At 1 T: r_L ≈ 0.24 m, ε ≈ 0.12. Adiabaticity weakening but collimation still effective.

At 0.1 T: r_L ≈ 2.4 m, ε ≈ 1.2. Adiabatic invariant broken. Particle detaches.

This analysis yields an effective mirror ratio of approximately R ≈ 10 (from 10 T throat to ~1 T detachment region) before non-adiabatic effects dominate. Beyond this point, particles go ballistic with whatever pitch angle they have at detachment.

2.5 Detachment Physics

The detachment process has two important characteristics that refine the idealized picture:

Gyrophase dependence. At ε ≈ 1, the particle's final pitch angle depends on its gyrophase at detachment. The result is a statistical spread around the mean detachment angle, not a clean cutoff. However, the particle retains the bulk of the parallel momentum it accumulated in the strong-field region. Detachment does not reverse collimation; it freezes it at a non-ideal but useful point.

Velocity-dependent smearing. Particles born with different ratios of perpendicular to parallel velocity detach at different field strengths. Low-v⊥ particles (born nearly parallel to the axis) have small Larmor radii and remain adiabatic deeper into the expansion, achieving excellent collimation. High-v⊥ particles detach earlier at lower effective mirror ratios. The exhaust angular distribution is therefore smeared: a superposition of well-collimated and less-well-collimated populations. For an initially isotropic distribution, this smearing degrades the directional efficiency below the idealized single-particle estimate.

Both effects reduce the directional efficiency from the idealized adiabatic prediction but do not eliminate the collimation advantage. The net effect is to bound the realistic directional efficiency to approximately 0.70–0.90, compared to the idealized 0.90–0.95 from the simple mirror formula.

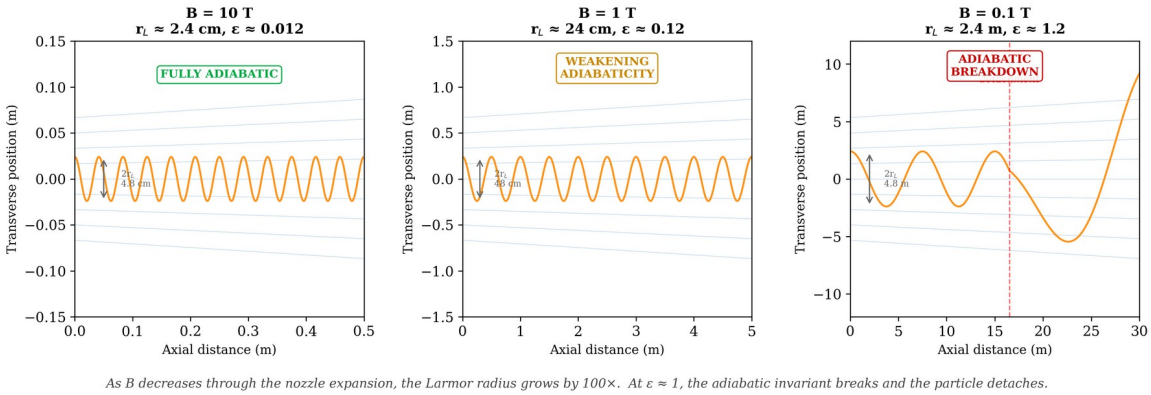

Figure 4. *Adiabatic breakdown of a 2.9 MeV alpha particle trajectory at three magnetic field strengths. Left: at 10 T (nozzle throat), the Larmor radius is 2.4 cm and the particle spirals tightly along field lines (ε ≈ 0.012, fully adiabatic). Center: at 1 T, the Larmor radius grows to 24 cm and adiabaticity weakens (ε ≈ 0.12). Right: at 0.1 T, the Larmor radius reaches 2.4 m and the adiabatic invariant breaks (ε ≈ 1.2), causing the particle to detach from the field lines and go ballistic. The effective mirror ratio is bounded at R ≈ 10 by this breakdown.*

3. System Architecture (Conceptual)

3.1 Fusion Core

The fusion core must sustain p-^{11}B reactions at temperatures exceeding 300 keV. No existing confinement concept has demonstrated net energy gain from p-^{11}B. The entire propulsion concept is conditional on this capability. Several approaches are under active development: TAE Technologies (field-reversed configurations), HB11 Energy (laser-driven ignition), and ENN (spherical torus).

A critical requirement is extraction of alpha products before thermalization. If the alphas equilibrate with the bulk plasma, the phase space advantage is lost. The relevant comparison is between the thermalization timescale and the transit time through the confinement region.

The Spitzer slowing-down time for a fast ion in a background plasma is approximately:

$$\tau_s \approx (3\sqrt{\pi}/4)(m_\alpha/m_e)^{1/2}(T_e/E_\alpha)^{3/2}\,\tau_e \quad (A)$$

For 2.9 MeV alphas in a p-^{11}B plasma at electron temperature $T_e \approx 300$ keV and density $\sim 10^{20}$ m^{-3}, the thermalization timescale is of order 10–100 μs. The transit time for a 0.039c alpha through a ~1 m confinement region is approximately 0.1 μs. The alphas therefore have two to three orders of magnitude of margin to exit the confinement region before significant energy exchange with the bulk plasma.

This margin is not unlimited. At higher plasma densities or longer confinement path lengths, thermalization becomes competitive with extraction. In the asymmetric mirror configuration described in Section 3.3, alphas born in the forward direction are reflected by the forward mirror and traverse the core a second time before exiting aft, approximately doubling their exposure to the bulk plasma. The 100–1000× timescale margin identified above is sufficient to accommodate this second pass. For open-field-line mirror geometries, the timescale separation remains favorable. The large Larmor radius of MeV alphas relative to the confining field structure further promotes decoupling from the bulk plasma.

3.2 Magnetic Nozzle

The magnetic nozzle converts angular spread to axial alignment. The mirror force:

$$F_\parallel = -\mu(\partial B/\partial s) \quad (8)$$

acts on particles with transverse velocity. Under the adiabatic approximation, the limiting half-angle is:

$$\sin(\theta) \approx 1/\sqrt{R} \quad (9)$$

As established in Section 2.4, the effective mirror ratio for 2.9 MeV alphas is bounded at approximately R ≈ 10 for nozzle gradient scale lengths of ~2 m, giving a mean half-angle of ~18° and directional efficiency of ~0.90 before accounting for smearing effects.

Two additional effects modify the single-particle picture. First, electrons remain magnetized much longer than alphas (their Larmor radius is smaller by a factor of ~85), creating an ambipolar electric field as the charge populations separate. This is the well-studied electron detachment problem in magnetic nozzle physics [23, 24]. The ambipolar field accelerates ions and decelerates electrons until they detach together, introducing corrections of order a few percent to the single-particle thrust estimates. Second, the plasma beta (β = P_kinetic/P_magnetic) varies along the nozzle. At the 10 T throat, β ≈ 0.06 and the magnetic field dominates, validating the single-particle adiabatic analysis. As the field drops through the expansion, β rises above unity in the detachment zone, consistent with the transition from magnetically guided to ballistic exhaust. The high-β regime at detachment does not invalidate the concept; it partially defines the detachment surface.

3.3 Capture Fraction and Asymmetric Mirror Configuration

The p-^{11}B reaction products are emitted isotropically in the center-of-mass frame. Although the alphas are born inside a magnetic topology and are immediately subject to the confining field, a symmetric configuration would lose approximately half the products out each end of the magnetic system. The parametric estimates in Section 4 assume near-complete capture. This requires an asymmetric mirror configuration.

The reference architecture uses a magnetic mirror with deliberately asymmetric mirror ratios. The forward end (toward the crew and payload) employs a high-ratio magnetic mirror: a single high-field superconducting coil producing a strong pinch that reflects the majority of alphas born in the forward direction back through the core and out the aft nozzle. The aft end is the diverging magnetic nozzle described in Section 3.2.

The forward mirror ratio determines the recapture fraction. At R_forward = 50 (requiring a forward coil at ~50 T if the core field is ~1 T), the fraction escaping forward is approximately $\sin^2(\theta) = 1/R = 2\%$. At R_forward = 20 (~20 T coil), the forward loss is ~5%. In either case, the vast majority of products are channeled aft through the nozzle, and the effective capture fraction approaches unity.

This configuration recovers the full 8.7 MeV per reaction for propulsion and preserves a conventional spacecraft layout: crew and structure forward, fusion core midship, nozzle aft, thrust along the main axis. It requires one additional high-field coil beyond the nozzle magnets but eliminates the need for magnetic elbows, dual nozzles, or complex exhaust routing.

The forward mirror field strength (20–50 T) is at the edge of current high-temperature superconducting magnet capability. Laboratory HTS magnets have demonstrated fields in this range, and the forward coil operates in a more favorable environment than the nozzle throat (no direct exposure to exhaust flux, static field geometry). The sensitivity of propellant fraction to capture efficiency is modest: even at R_forward = 10 (10% forward loss), the propellant fractions increase by only ~1–2 percentage points above the estimates in Section 4.

A subtlety arises with the perpendicular-born population: alphas created with velocity vectors near $\pi/2$ to the axis have almost all $v_\perp$ and almost no $v_\parallel$. These are exactly the particles that magnetic mirrors trap most effectively. Rather than escaping through either end, they bounce between the forward mirror and the nozzle throat indefinitely. Extraction of this population depends on a race between two timescales: pitch-angle scattering into the loss cone (which allows escape into the nozzle) and thermalization via Coulomb collisions with the bulk plasma (which degrades the non-thermal advantage). A particle bouncing many times accumulates scattering events from both processes.

Several architectural options exist for managing the trapped population. Active RF loss-cone pumping could use ion cyclotron waves to scatter trapped particles into the loss cone, deliberately destabilizing their orbits. Asymmetric midplane field shaping could cause trapped-particle drift orbits to migrate axially toward the nozzle end over successive bounces. Lowering the midplane field widens the loss cone, reducing the number of scattering events needed for escape at the cost of reduced confinement quality. Alternatively, the trapped fraction could simply be accepted as a loss and folded into the directional efficiency as a capture penalty. The quantitative impact of each approach is a primary output of the particle-tracing simulation described in Section 6.1.

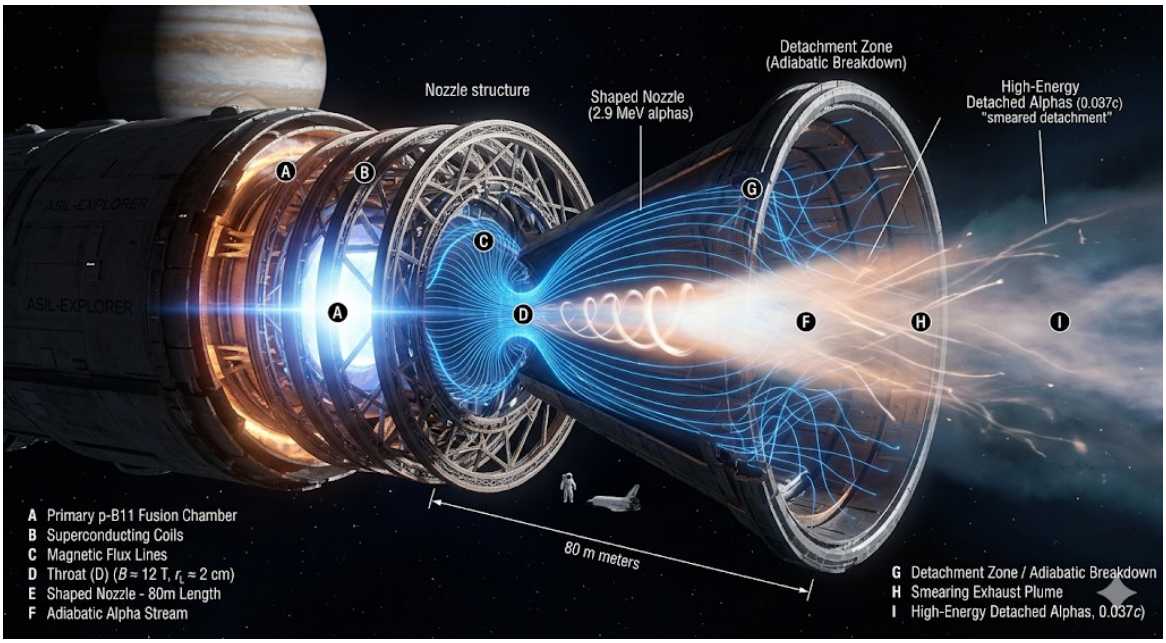

Figure 1. *Conceptual rendering of a p-¹¹B directed exhaust propulsion system in the asymmetric mirror configuration described in Section 3.3. The fusion core (A) generates 2.9 MeV alpha particles. A high-field forward mirror (not shown, forward of A) reflects aft-bound products back through the core. Products are collimated through a shaped magnetic nozzle (E, ~80 m length) supported by superconducting coils (B). The throat (D) operates at ~12 T with a Larmor radius of ~2 cm. Adiabatic collimation is effective through the nozzle body (F) until the detachment zone (G) where ε ≈ 1 and the invariant breaks. Beyond detachment, the exhaust forms a smeared plume (H) of high-energy alphas (I) at approximately 0.037c. Image generated by Gemini (Google DeepMind).*

3.4 Contrast with Prior Work

The closest prior work in the academic literature is Tarditi's NASA NIAC Phase I study [12]. Tarditi assumed an aneutronic source and investigated beam conditioning for propulsion. His architecture deliberately thermalizes the products: alphas are injected non-adiabatically into a magnetic duct, transfer energy into gyro-motion, and heat a denser propellant expanded through a magnetic nozzle. This is a fusion-heated thermal rocket.

In the informal literature, MatterBeam's ToughSF analysis [22] is the most detailed public attempt to explain the Epstein Drive from The Expanse using real physics. That analysis uses D-He3 fuel with inertial confinement (laser-ignited pellets) and a modified VISTA architecture, achieving approximately 75% thrust efficiency through shaped fusion charges and magnetic redirection. The ToughSF treatment is valuable as an engineering feasibility sketch but differs from the present work in three respects: it uses D-He3 rather than p-¹¹B (retaining some neutron production from D-D side reactions), it does not address the phase space structure of the products or the Liouville constraint, and it does not quantify the adiabatic limits on magnetic collimation.

The approach proposed here is distinct from both: preserve the non-thermal character of p-^{11}B products and redirect them directly, avoiding both thermalization (Tarditi) and shaped-charge inertial schemes (ToughSF). The phase space argument in Section 2 provides the theoretical basis for why direct redirection is favorable for p-^{11}B specifically. To our knowledge, this argument has not been made in the prior literature.

4. Parametric Estimates

The following estimates define the target design space. They are not predictions. Each depends on assumptions that require validation through simulation.

4.1 Effective Exhaust Velocity

Directional efficiency η_d represents the fraction of exhaust kinetic energy contributing to axial thrust:

$$\eta_d = \langle \cos\theta \rangle^2 \quad (10)$$

$$v_e = v_a \times \sqrt{\eta_d} \quad (11)$$

For $v_a = 0.039c$:

Table 1: Effective Exhaust Velocity vs. Directional Efficiency

Scenario	η_d	v_e
Idealized (R=50)	0.95	0.038c
Adiabatic limit (R≈10)	0.90	0.037c
With smearing effects	0.70–0.85	0.033–0.036c

4.2 Comparison with D-T

For propulsion, the relevant metric is directed energy: how much reaction energy converts to steerable axial momentum.

D-T releases 17.6 MeV, but 80% (14.1 MeV) goes to an uncharged neutron. The steerable alpha carries 3.5 MeV. In terms of rest mass, the directed fraction is approximately 0.20 × 0.378% ≈ 0.076%.

p-^{11}B releases 8.7 MeV, 100% in charged products. The directed fraction is 100% of 0.078% ≈ 0.078%.

The two fuels produce comparable directed energy per unit fuel mass. But D-T additionally requires neutron shielding, thermal conversion hardware, radiators, and a secondary propulsion system. A fair comparison requires a full system mass model, which this paper does not provide. The p-^{11}B advantage may be primarily in system simplicity rather than raw energy metrics.

Table 2: Energy Partition Comparison

Parameter	D-T	p-^{11}B
Total energy	17.6 MeV	8.7 MeV
Mass-energy conversion	0.378%	0.078%
Charged fraction	20%	100%
Directed energy (% rest mass)	~0.076%*	~0.078%†
Neutron shielding	Significant	Negligible
Thermal conversion	Required (80%)	Not required

** Before thermal conversion losses. Actual directed fraction after Carnot cycle is lower.*

† Before nozzle collimation losses. Actual directed fraction depends on η_d.

4.3 Mass Ratio Estimates

$$m_0/m_f = \exp(\Delta v/v_e) \quad (12)$$

For a 10-day Earth-Jupiter brachistochrone ($\Delta v \approx 0.012c$):

Table 3: Mass Ratio Sensitivity

Scenario	v_e	Propellant %
Idealized	0.038c	27%
Adiabatic limit	0.037c	28%
With smearing	0.033–0.036c	28–31%
Severe degradation	0.025c	38%

The concept is robust to the adiabatic breakdown identified in Section 2.4. The efficiency enters through a square root ($\eta_d^{1/2} \rightarrow v_e$), and the rocket equation is logarithmic in v_e. These two layers of compression insulate the propellant fraction against moderate efficiency losses. The concept would require catastrophic degradation ($\eta_d < 0.3$) before propellant fractions become operationally prohibitive.

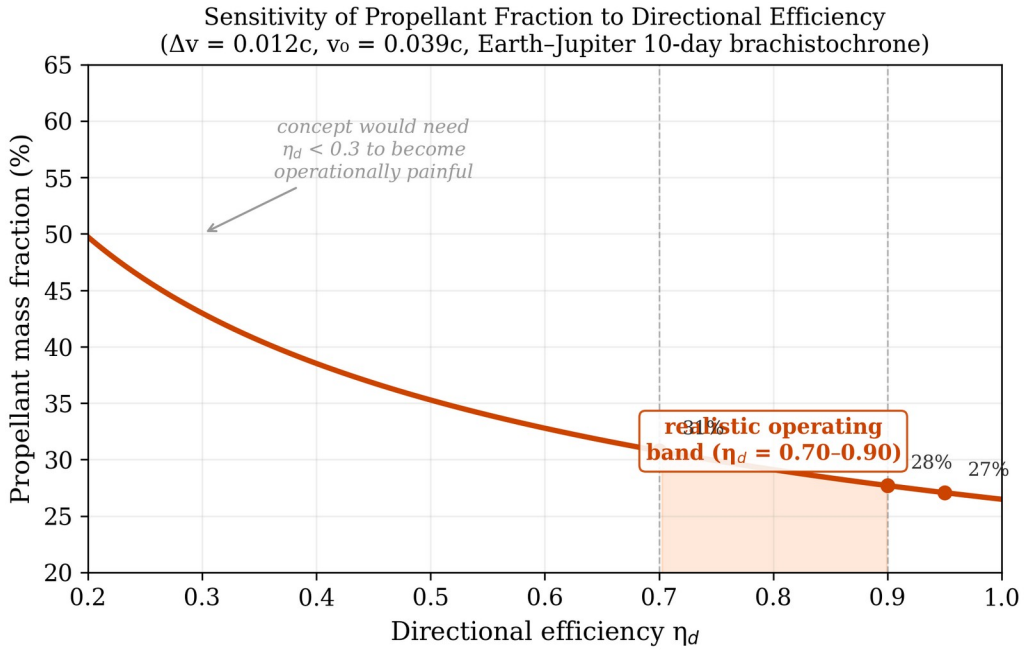

Figure 5. *Sensitivity of propellant mass fraction to directional efficiency for the reference mission (Δv = 0.012c, v_0 = 0.039c). The curve is nearly flat in the realistic operating band (η_d = 0.70–0.90), with propellant fraction varying only from 31% to 28%. This insensitivity arises from two layers of mathematical compression: efficiency enters the exhaust velocity through a square root, and exhaust velocity enters the mass ratio through a logarithm. The concept would need to fail catastrophically (η_d < 0.3) for propellant fractions to become operationally prohibitive.*

4.4 Power Requirements

The power requirement scales directly with the mission acceleration profile. For a 1000-tonne spacecraft:

30-day Earth-Jupiter transfer (~0.14g continuous): This near-term mission profile requires thrust of ~1.4×10^6 N and jet power of approximately 0.8 TW. This is an enormous power level by current standards but falls within the range of conceivable future energy systems, particularly if fusion power density improves along the trajectory suggested by current research programs.

10-day Earth-Jupiter transfer (~0.43g continuous): The reference mission used throughout this paper requires thrust of ~4.2×10^6 N and jet power of approximately 25 TW, comparable to twice the current global installed nuclear capacity. This represents the asymptotic performance limit of the concept, not a near-term target.

$$F = ma; \quad P\_jet = Fv\_e/2 \quad (15)$$

These power levels are inherent to the mission profiles, not specific to any propulsion technology. Any system delivering continuous high-g thrust at relativistic exhaust velocities must

sustain comparable output. The propulsion architecture described in this paper does not change the power requirement; it changes the fraction of that power that becomes useful thrust.

Table 4: Propellant Fractions by Propulsion System (10-day Jupiter)

System	Propellant Fraction
Chemical (LOX/LH2)	>99% (infeasible)
Nuclear thermal	>95% (infeasible)
D-T fusion (thermal)	60–97%
p-¹¹B directed exhaust (this paper)	28–31% (estimated)
Antimatter (theoretical limit)	~2%

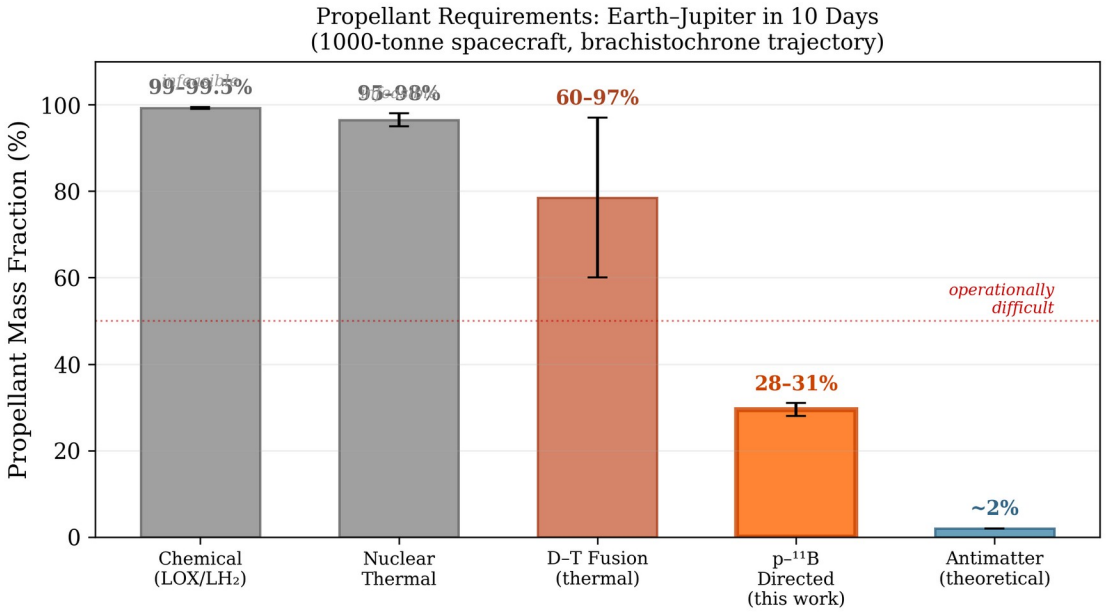

Figure 6. *Propellant mass fractions for a 10-day Earth–Jupiter brachistochrone transfer across propulsion technologies. Chemical and nuclear thermal systems require propellant fractions exceeding 95%, rendering the mission infeasible. D–T fusion with thermal exhaust spans a wide range (60–97%) depending on assumptions about thermal conversion efficiency. The p-¹¹B directed exhaust architecture proposed in this paper estimates 28–31%, below the operational difficulty threshold. Only antimatter propulsion (~2%) offers superior performance, but requires fuel that does not exist in macroscopic quantities.*

5. What This Paper Does Not Establish

The following are not established by the arguments in this paper:

Nozzle performance from simulation. No particle-tracing or PIC simulation has been performed. The adiabatic analysis in Section 2.4 provides order-of-magnitude bounds but does not capture

non-adiabatic transition dynamics, loss cone effects, or the full velocity-dependent smearing of the detachment surface. The magnitude of performance degradation from these effects is unknown.

Bremsstrahlung budget. Proton-boron plasmas suffer significant bremsstrahlung losses due to boron's atomic number (Z=5) and the high temperatures required for ignition. The bremsstrahlung power can approach or exceed fusion power under unfavorable conditions. This paper does not present a radiation loss budget. This is one of the most well-studied objections to p-^{11}B fusion and cannot be dismissed.

Three-body energy distribution. The alpha energy spread is characterized here as ~±25%. The actual distribution is governed by the Dalitz plot including ^{8}Be resonance structure. Proper treatment requires the measured differential cross-section as initial conditions for particle tracing.

Thermalization avoidance. The concept depends on extracting products before thermalization. Section 3.1 estimates a timescale margin of 100–1000×, but in the asymmetric mirror configuration, forward-reflected alphas traverse the core twice. Whether the reflected population retains sufficient non-thermal character depends on the core density, path length, and magnetic topology. The paper estimates that the margin accommodates the double pass but does not model this explicitly.

System mass comparison. The directed-energy comparison (Table 2) is suggestive but incomplete. A fair comparison with D-T requires a full system mass model including shielding, conversion hardware, radiators, and structural mass.

Space charge limits. At the reference mission mass flow rate of 0.36 kg/s of He^{2+}, the ion flux is approximately 5.4×10^{25} ions/s, corresponding to a beam current of ~17 MA. Even distributed over a 100 m² cross-section, the current density is ~170 kA/m². At this scale, beam self-field effects and Child-Langmuir space charge limits are non-trivial and may compete with magnetic collimation. Whether co-moving electrons from the fusion plasma provide sufficient neutralization is unknown. This requires self-consistent PIC simulation (see Section 6.3) and is not resolved by the present analysis.

Nozzle capture fraction. The parametric estimates assume near-complete capture via the asymmetric mirror configuration described in Section 3.3. The forward mirror ratio required ($R \approx 20–50$) is at the edge of current HTS capability. If the forward mirror underperforms, the capture fraction degrades and propellant fractions increase. At R_forward = 10 (10% forward loss), the impact is ~1–2 percentage points. Without a forward mirror entirely (50% capture), propellant

fractions rise to ~35–40%. The concept survives across this range but the forward mirror field strength should be validated against foreseeable magnet technology.

Trapped perpendicular population. Alphas born near π/2 to the axis are trapped between the forward mirror and nozzle throat, bouncing indefinitely until they either scatter into the loss cone (useful) or thermalize (wasted). The fraction of the isotropic birth distribution that falls into this trapped regime, the average number of bounces before loss-cone escape, and the cumulative thermalization during those bounces are not quantified in this paper. This is the most architecturally consequential open question identified in Section 3.3 and is a primary target for the particle-tracing simulation in Section 6.1.

Each item above is a well-defined computational or analytical problem: particle tracing, radiation transport, kinetic simulation, system mass modeling. None requires new physics. None requires experimental hardware. These are exactly the class of high-dimensional optimization and simulation problems where autonomous research systems will deliver the fastest progress. The list of what this paper does not establish is, in effect, the work order for the AGI/ASI research programs now being built.

6. Proposed Research Program

If the concept is to be validated or falsified, the following work is required:

6.1 Particle-Tracing Simulation (Highest Priority)

A particle-tracing simulation using the actual three-body energy and angular distribution through a realistic magnetic nozzle geometry. This should report the resulting axial momentum distribution, directional efficiency, particle loss fraction, and the dependence on field geometry parameters. This single study would convert the conceptual argument into a quantitative result or reveal that the idealized estimates are unachievable.

6.2 Bremsstrahlung and Radiation Budget

A self-consistent power balance model including bremsstrahlung, synchrotron radiation, and secondary neutron production from side reactions. This determines whether positive energy balance is achievable and what fraction of fusion power is available for directed exhaust.

6.3 Space Charge Analysis

Self-consistent modeling of beam transport including space charge effects at propulsion-relevant flux densities.

6.4 System Mass Model

A comparative model for D-T thermal, D-T with direct conversion, and p-^{11}B directed exhaust, including all parasitic mass.

6.5 Confinement-Extraction Integration

Co-design of the interface between the fusion core, the forward mirror, and the aft magnetic nozzle. In the asymmetric mirror architecture (Section 3.3), the forward mirror must be strong enough to reflect most forward-born alphas while the aft nozzle throat must accept the combined flux of directly aft-born and reflected products. The core magnetic topology must simultaneously sustain ignition conditions and allow rapid product extraction without quenching the plasma or contaminating the exhaust stream with thermal ions.

7. Engineering Research Directions for ASI-Enabled Development

The physics question (does the phase space argument hold quantitatively?) is separable from the engineering question (can a system be built that exploits it?). This section catalogs the principal engineering challenges, each framed as a tractable optimization problem suited to autonomous research systems.

7.1 Magnetic Nozzle Geometry Optimization

The adiabatic limit identified in Section 2.4 is not fixed. It depends on the field gradient profile. A simple diverging solenoid produces steep gradients ($\nabla B \sim 1/z^3$ in the far field), forcing early detachment. Shaped field profiles using secondary trim coils downstream of the main throat can stretch the gradient scale length L_B, keeping ε small deeper into the expansion and recovering a higher effective mirror ratio.

The trade-off is physical scale: stretching L_B to ~10 m at 0.05 T requires coil structures and truss extending tens of meters, with bore radii exceeding the local Larmor radius (~5 m at those field strengths). Whether the mass of extended nozzle structure exceeds the propellant mass saved by improved efficiency is a parametric design question. The answer depends on coil technology

(current density, structural mass per meter), mission profile (how much propellant savings is worth how much dry mass), and spacecraft architecture constraints.

A rough estimate establishes the scale of the trade. High-temperature superconducting coils at the 10+ T class run approximately 10–50 kg per meter of bore circumference. A single coil with a 10-meter bore diameter weighs roughly 300–1500 kg. A nozzle assembly of five coils would mass 1.5–7.5 tonnes. For a 1000-tonne spacecraft on the 30-day mission profile (~300 tonnes propellant), a 5-tonne engine mass is a 1.7% penalty on the total mass budget. This is comparable to the propellant savings from improving η_d from 0.70 to 0.90 (~3% propellant). The implication is that the optimal design sits at a moderate mirror ratio (R ≈ 15–20) where the marginal coil mass equals the marginal propellant savings. Finding this sweet spot is a primary objective of the parametric simulation proposed in Paper 2.

This is a high-dimensional, non-convex optimization over field geometry, coil placement, current profiles, and structural mass. The design space includes not only the aft nozzle expansion coils but also the forward mirror coil: its field strength determines the capture fraction (Section 3.3), while its mass contributes to the engine budget. The optimization likely contains a sweet spot at moderate aft mirror ratios (R ≈ 15–20) with a forward mirror ratio of R ≈ 20–50, where modest field shaping yields most of the recoverable efficiency without extreme physical scale. This is exactly the class of problem where AI-driven parameter space exploration outperforms human-guided iteration.

7.2 Bremsstrahlung Management

Bremsstrahlung losses in p-¹¹B plasmas are a fundamental challenge to ignition and sustained operation. Several mitigation strategies have been proposed in the literature: maintaining non-thermal ion distributions to reduce electron heating, operating at electron temperatures well below ion temperatures through alpha channeling, and exploiting non-equilibrium plasma states that reduce the effective bremsstrahlung rate. Each of these involves complex plasma dynamics that are difficult to optimize analytically but amenable to computational exploration.

7.3 Thermalization Avoidance

Preserving the non-thermal character of alpha products requires that they exit the confinement region before significant energy exchange with the bulk plasma. In the asymmetric mirror configuration, forward-reflected alphas traverse the core twice, doubling their thermalization exposure relative to directly aft-born products. The timescale margin estimated in Section 3.1 (100–1000×) is sufficient to accommodate this, but the double-pass creates a population of alphas

with slightly degraded non-thermal character compared to the single-pass population. Quantifying the velocity distribution of reflected versus direct alphas at the nozzle throat is a specific output of the particle-tracing simulation in Section 6.1. Designing a confinement system that simultaneously achieves ignition conditions and rapid product extraction is a co-optimization problem.

7.4 Thermal Management and Heat Rejection

Even with high directional efficiency, residual losses from imperfect collimation, bremsstrahlung, and secondary radiation must be rejected as waste heat. For a 25 TW system with 5% thermal losses, the waste heat load is ~1.25 TW, requiring radiator areas of order 10^4 m² at typical spacecraft radiator temperatures. Advanced radiator concepts (droplet radiators, high-emissivity surfaces, phase-change systems) reduce but do not eliminate this requirement. Radiator mass and area may be a binding constraint on continuous high-power operation.

Additionally, nozzle structural elements and superconducting coils must be shielded from or positioned to avoid direct line-of-sight to the fusion core's bremsstrahlung emission. The diverging nozzle geometry is partially favorable here, as downstream coils sit far from the axis and can be shadowed by the core structure itself. Localized X-ray shielding (tungsten, lead) adds mass but is confined to specific sightlines. The bremsstrahlung heat load on structure is geometry-dependent and must be addressed in the integrated system design.

7.5 Materials and Structural Design

The nozzle throat region experiences intense particle flux, magnetic stress, and thermal loading. Material selection for components in direct exposure to MeV alpha particles is a specialized problem. The nozzle structural elements must maintain alignment precision under thermal cycling and magnetic forces. Zero-gravity assembly and deployment of large magnetic nozzle structures (potentially tens of meters in length) is an operational challenge that intersects with ongoing work in large-scale space construction.

7.6 Fuel Handling and Supply Chain

Boron-11 constitutes 80% of natural boron, which is geologically abundant. Hydrogen is ubiquitous. Neither fuel component is exotic or scarce. The engineering challenge is fuel handling at propulsion-relevant mass flow rates (~0.36 kg/s for the reference mission) in the form suitable for injection into the fusion core. This includes ionization, acceleration to confinement-relevant energies, and precise delivery to the reaction zone.

7.7 The Role of Autonomous Research

Several of the above problems share a common structure: high-dimensional parameter spaces, coupled physics across multiple scales, and performance landscapes with many local optima. This is the regime where autonomous research systems offer the greatest advantage over human-guided exploration. Specific applications include: parametric optimization of nozzle field geometry against mass and efficiency; search over confinement topologies for configurations that simultaneously achieve ignition and rapid product extraction; iterative design of thermal management systems under coupled radiation, conduction, and structural constraints; and co-optimization of the full system (core, nozzle, radiators, structure) against mission performance metrics.

Beyond the exhaust architecture, the ignition problem itself contains unexplored pathways amenable to autonomous exploration. Crystal channeling in boron lattices could extend effective proton range by 10–100×, improving beam-target hit rates without increasing beam power. Muon-catalyzed p-^{11}B fusion could eliminate the ignition temperature requirement entirely, enabling room-temperature reactions if the alpha-sticking problem can be solved. These represent concrete, experimentally testable hypotheses in a vast and largely untouched parameter space of tunneling enhancement, screening effects, and lattice-mediated nuclear reactions.

The engineering challenges cataloged here are not objections to the physics of the concept. They are the research program that follows from it.

8. Broader Context

This paper is motivated by a forecast: the pace of scientific research will accelerate dramatically, driven by increasingly autonomous AI systems. This is not speculative in the sense of predicting new physics. It is an extrapolation of trends already visible.

If this forecast is approximately correct, research prioritization becomes the binding constraint. The question is not whether hard problems will be solved, but which problems should be worked on now so solutions are available when needed.

Ignition is the long pole. Achieving p-^{11}B ignition is extremely difficult with current methods, but it is exactly the class of problem (high-dimensional plasma optimization) where autonomous research systems will achieve the fastest progress. If AGI-class systems are available within 1–10 years, p-^{11}B ignition becomes plausible on a similar timescale.

The architecture is separable. Exhaust handling (nozzle design, thermal management, fuel handling) can be developed independently of the fusion core. Waiting for ignition before beginning this work wastes lead time.

The application is time-sensitive. Infrastructure decisions in the next decade (lunar bases, Martian settlements, asteroid mining) will be shaped by assumptions about available propulsion. If directed p-^{11}B exhaust is feasible, it changes the optimal architecture for interplanetary logistics. That information is needed before the infrastructure is built.

ASI as the engineering accelerant. The hardest component of this propulsion system is p-^{11}B ignition: a high-dimensional plasma optimization problem that has resisted decades of conventional research. This is precisely the class of problem where autonomous research systems offer the greatest leverage. ASI-enabled laboratories on Earth, running hypercompressed engineering iteration cycles, could explore the confinement design space at a pace impossible for human-led programs. The propulsion architecture described in this paper should be developed in parallel so that when ignition is achieved, the downstream system is ready to exploit it. The result is not a propulsion system that serves ASI; it is a propulsion system that ASI makes possible.

9. Conclusion

Proton-boron fusion products have a phase space structure qualitatively more favorable for direct magnetic collimation than thermal plasmas. Their entropy is concentrated in angular distribution rather than momentum magnitude. Magnetic nozzle geometries can collimate the exhaust by trading angular spread for spatial spread, consistent with Liouville's theorem, placing the conserved phase space volume in a degree of freedom irrelevant to thrust.

Adiabatic analysis establishes that collimation is physically effective at mirror ratios up to ~10, bounded by the Larmor radius of 2.9 MeV alphas in the diverging field region. Beyond this ratio, particles undergo non-adiabatic detachment with gyrophase-dependent and velocity-dependent smearing of the exhaust angle. The resulting directional efficiencies of 70–90% yield estimated propellant mass fractions of 28–31% for a 10-day Earth-Jupiter transfer. The concept is robust to moderate efficiency degradation because the efficiency enters through a square root and the rocket equation is logarithmic in exhaust velocity.

The concept is situated within a broader context: accelerating autonomous research capability will address the hardest component (p-^{11}B ignition), while the exhaust architecture can be developed in parallel. If validated, this concept would enable propulsion performance currently accessible only to hypothetical antimatter systems, using abundant, non-exotic fuel.

The question this paper poses to the community is whether the phase space argument developed here is quantitatively sufficient to justify a dedicated simulation and design effort. We have tried to state the uncertainties clearly enough that readers can form their own judgment.

Acknowledgments

Iterative development and computational analysis of arguments in this paper were conducted with assistance from Claude Opus 4.6 (Anthropic), Gemini 3.1 Pro (Google DeepMind), and GPT-5.4 (OpenAI). The adiabatic limit analysis in Section 2.4 and the detachment physics in Section 2.5 were refined through adversarial dialogue with Gemini and Opus 4.5 (intentionally), which provided the magnetic rigidity calculations and identified the velocity-dependent smearing of the detachment surface. The concept rendering in Figure 1 was generated by Gemini. All substantive claims, interpretive judgments, and errors are the sole responsibility of the author(s).

References

[1] Rostoker, N., Binderbauer, M.W., and Monkhorst, H.J. (1997). "Colliding Beam Fusion Reactor." Science, 278(5342), 1419–1422.

[2] Putvinski, S.V., Ryutov, D.D., and Yushmanov, P.N. (2019). "Fusion reactivity of the pB11 plasma revisited." Nuclear Fusion, 59(7), 076018.

[3] Nevins, W.M. and Swain, R. (2000). "The thermonuclear fusion rate coefficient for p-^{11}B reactions." Nuclear Fusion, 40(4), 865.

[4] Rider, T.H. (1997). "Fundamental limitations on plasma fusion systems not in thermodynamic equilibrium." Physics of Plasmas, 4(4), 1039–1046.

[5] Liu, S. et al. (2025). "Feasibility of proton–boron fusion under non-thermonuclear steady-state conditions: Rider's constraint revisited." Physics of Plasmas, 32(1), 012101.

[6] Putvinski, S.V. et al. (2024). "Lowering the reactor breakeven requirements for proton–boron 11 fusion." Physics of Plasmas, 31(1), 012503.

[7] Ahlstrom, H.G. (1982). "Magnetic Nozzle Design for Plasma Propulsion." AIAA Journal, 20(7), 971–977.

[8] Santarius, J.F. (1998). "Magnetic Fusion for Space Propulsion." Fusion Technology, 33(1), 28–39.

[9] Atzeni, S. and Meyer-ter-Vehn, J. (2004). The Physics of Inertial Fusion. Oxford University Press.

[10] Borowski, S.K. (1995). "Comparison of Fusion/Antiproton Propulsion Systems for Interplanetary Travel." NASA TM-107030.

[11] Kammash, T. (1995). Fusion Energy in Space Propulsion. AIAA Progress in Astronautics and Aeronautics, Vol. 167.

[12] Tarditi, A.G., Scott, J.H., and Miley, G.H. (2012). "Aneutronic Fusion Spacecraft Architecture." NASA NIAC Phase I Final Report.

[13] Hyde, R.A. et al. (1991). "VISTA: A Vehicle for Interplanetary Space Transport Application Powered by Inertial Confinement Fusion." LLNL Report UCRL-ID-107066.

[14] Hora, H. et al. (2017). "Fusion energy using avalanche increased boron reactions for block-ignition by ultrahigh power picosecond laser pulses." Laser and Particle Beams, 35(4), 730–740.

[15] Eliezer, S. and Martinez-Val, J.M. (1998). "Proton-boron-11 fusion reactions induced by heat-detonation burning waves." Laser and Particle Beams, 16(4), 581–598.

[16] Sikora, M.H. and Woo, H.J. (2016). "A new evaluation of the p+^{11}B reaction rates." Nuclear Physics A, 945, 1–13.

[17] Stave, S. et al. (2011). "Understanding the ^{11}B(p,α)αα reaction at the 0.675 MeV resonance." Physics Letters B, 696(1–2), 26–29.

[18] Binderbauer, M.W. et al. (2015). "A high performance field-reversed configuration." Physics of Plasmas, 22(5), 056110.

[19] Chapman, J.J. (2011). "Advanced Fusion Reactors for Space Propulsion and Power Systems." NASA Technical Report.

[20] Goldston, R.J. and Rutherford, P.H. (1995). Introduction to Plasma Physics. CRC Press.

[21] van der Linden, S. et al. (2023). "First measurements of p^{11}B fusion in a magnetically confined plasma." Nature Communications, 14, 1077.

[22] MatterBeam (2019). "The Expanse's Epstein Drive." ToughSF Blog. Available at: http://toughsf.blogspot.com/2019/10/the-expanses-epstein-drive.html

[23] Ahedo, E. and Merino, M. (2010). "Two-dimensional supersonic plasma acceleration in a magnetic nozzle." Physics of Plasmas, 17(7), 073501.

[24] Merino, M. and Ahedo, E. (2016). "Magnetic nozzle plasma exhaust simulation for the VASIMR thruster." Proceedings of the 52nd AIAA Joint Propulsion Conference.

Appendix A: Derivation of Key Relations

A.1 Alpha Particle Velocity

$$v = c\sqrt{(1 - (mc^2/(T + mc^2))^2)} \quad (A1)$$

For m_ac^2 = 3727.4 MeV, T = 2.9 MeV: v ≈ 0.039c.

A.2 Mass-Energy Conversion

$$f = Q / (m\_reactants \times c^2) \quad (A2)$$

p-^{11}B: 8.7/11,190.8 ≈ 0.078%. D-T: 17.6/4,684.5 ≈ 0.376%.

A.3 Magnetic Rigidity and Larmor Radius

For He^{2+} at 2.9 MeV: m = 6.64 × 10^{-27} kg, q = 3.22 × 10^{-19} C, v ≈ 1.18 × 10^7 m/s.

$$r\_L = mv/(qB) \approx 0.24/B \text{ meters} \quad (A3)$$

At 10 T: 2.4 cm. At 1 T: 24 cm. At 0.1 T: 2.4 m.

A.4 Adiabaticity Parameter

$$\varepsilon = r\_L/L\_B \quad (A4)$$

Adiabatic invariant conserved when ε ≪ 1. For L_B = 2 m: ε crosses unity near B ≈ 0.1 T, establishing the effective mirror ratio at R ≈ 10.

A.5 Specific Impulse

$$I\_sp = v\_e/g\_0 \approx 1.17 \times 10^7/9.81 \approx 1.19 \times 10^6 \text{ s} \quad (A5)$$